

Article

Assembly of CaIn_2S_4 on Defect-Rich BiOCl for Acceleration of Interfacial Charge Separation and Photocatalytic Phenol Degradation via S-Scheme Electron Transfer Mechanism

Zhuangzhuang Zhang ^{1,†}, Yuanyuan Zhang ^{1,†}, Xuanxuan Han ¹, Li Guo ¹, Danjun Wang ^{1,2,*} and Kangle Lv ^{3,*} 

¹ Shaanxi Key Laboratory of Chemical Reaction Engineering, College of Chemistry and Chemical Engineering, Yan'an University, Yan'an 716000, China; zhzyyau@163.com (Z.Z.); zyy185202@163.com (Y.Z.); hanxuanxuan@yau.edu.cn (X.H.); guoli20052017@163.com (L.G.)

² Chongqing Key Laboratory of Inorganic Special Functional Materials, College of Chemistry and Chemical Engineering, Yangtze Normal University, Chongqing 408100, China

³ College of Resources and Environmental Science, South-Central University for Nationalities, Wuhan 430074, China

* Correspondence: wangdj761118@yau.edu.cn (D.W.); lvkangle@mail.scuec.edu.cn (K.L.)

† These authors contributed equally to this work.

Abstract: The novel 2D/2D S-scheme heterostructure of BiOCl nanosheets coupled with CaIn_2S_4 nanosheets ($\text{CaIn}_2\text{S}_4/\text{BiOCl-SOVs}$), which contains surface oxygen vacancies (SOVs), has been successfully prepared by high-temperature calcination combined with a solvothermal synthetic strategy. Under visible-light irradiation, the apparent rate constant ($K_{\text{app}}/\text{min}^{-1}$) for phenol degradation on the 1 wt% $\text{CaIn}_2\text{S}_4/\text{BiOCl-SOVs}$ photocatalyst is about 32.8 times higher than that of pure BiOCl. The superior performance was attributed to the synergistic effect between the SOVs, CaIn_2S_4 , and BiOCl, which can effectively narrow the bandgap and accelerate the interfacial charge separation of $\text{CaIn}_2\text{S}_4/\text{BiOCl-SOVs}$ heterojunctions. Subsequently, it significantly promotes the generation of superoxide radicals (O_2^-), hydroxyl radicals, and h^+ , which participate in the photodegradation process of phenol. The catalyst still maintained a relatively high activity after repeated tests as a demonstration of its photostability. This work successfully proposed an efficient method to design a new 2D/2D S-scheme heterostructure with SOVs as possible photocatalysts in the field of environmental remediation.

Keywords: in-situ assembly; $\text{CaIn}_2\text{S}_4/\text{BiOCl-SOVs}$; 2D/2D heterostructure; phenol degradation



Citation: Zhang, Z.; Zhang, Y.; Han, X.; Guo, L.; Wang, D.; Lv, K. Assembly of CaIn_2S_4 on Defect-Rich BiOCl for Acceleration of Interfacial Charge Separation and Photocatalytic Phenol Degradation via S-Scheme Electron Transfer Mechanism. *Catalysts* **2021**, *11*, 1130. <https://doi.org/10.3390/catal11091130>

Academic Editor: Christos Trapalis

Received: 9 August 2021

Accepted: 18 September 2021

Published: 20 September 2021

Publisher's Note: MDPI stays neutral with regard to jurisdictional claims in published maps and institutional affiliations.



Copyright: © 2021 by the authors. Licensee MDPI, Basel, Switzerland. This article is an open access article distributed under the terms and conditions of the Creative Commons Attribution (CC BY) license (<https://creativecommons.org/licenses/by/4.0/>).

1. Introduction

During the past few decades, with the rapid development of modern industrial and agricultural technology, energy and environmental issues have become important topics on a global level [1–4]. The treatment of sewage, which is a cause for widespread concern, has become the top priority of environmental protection work. Sewage can be differentiated according to the pollution source: industrial wastewater, non-recyclable water used in life, and sewage caused by commercial development. Industrial wastewater is the most harmful, in which the concentration of organic matter has gradually increased, and whose components have become increasingly complex, resulting in a more difficult degradation process and in challenging and often unsuccessful removal efforts by a number of applied technologies. Consequently, new sewage treatment technologies need to be developed. The removal of highly toxic and persistent organic pollutants contained in wastewater by employing semiconductor photocatalysis technology can be used as an attractive method to solve the problem of environmental water pollution. This technology has demonstrated unique advantages, including high efficiency, favorable economy, green and sustainable aspects, and environmental protection [5–12]. Therefore, it is particularly important to develop a photocatalyst with high catalytic performance in the degradation of pollutants in

sewage. As a valuable p-type photocatalyst, bismuth oxychloride (BiOCl) has been extensively studied due to its good acid and alkali resistance, strong photostability, non-toxicity to organisms, simple preparation, and its functionality as a relatively positive valence band oxidation site. However, pure BiOCl cannot absorb visible light due to its wide bandgap and exhibits poor solar energy utilization in practical applications [13–15]. Therefore, the important question in current investigations has emerged on how to effectively broaden the response to visible light and realize the improvement of the visible-light photocatalytic activity of BiOCl [16–19]. Recently, many modification methods have been devoted to address these problems, such as modifications to generate surface oxygen vacancies (SOVs) and the construction of a compact heterojunction structure. The introduction of SOVs in photocatalysts through high-temperature calcination treatment resulted in some positive and unexpected results for the visible-light photocatalytic performance [20–24]. Fu et al. reported an improved photocatalytic activity by, i.a., narrowing the bandgap through introducing SOVs on bismuth molybdate (Bi_2MoO_6) grafted with Fe(III) clusters via a reliable calcination process combined with an impregnation approach. Lu et al. [8] used a simple in-situ modified sol-gel method to synthesize single crystals of mesoporous C-doped titanium dioxide (TiO_2) with oxygen vacancies, in which the presence of oxygen vacancies led to a low carrier recombination rate and enhanced carrier separation, which finally promoted the degradation of organic pollutants. A resemblance was gained for BiOCl in Gao's group.

In addition, the preparation of heterojunction photocatalysts as an effective means to improve photocatalytic performance has also received considerable attention in various applications of photocatalysis [25–27]. However, the ability of heterostructures constructed by randomization to ameliorate the efficiency of light absorption and photogenerated carrier separation is not particularly satisfactory. Hence, a special heterojunction design has to be formulated to further improve photocatalytic activity. In recent years, 2D/2D heterojunctions composed of 2D nanosheet-like structures have shown certain advantages for improving photogenerated carrier separation due to the tight heterojunction interface effect [28,29]. The calcium indium sulfide CaIn_2S_4 is a ternary AB_2X_4 sulfur group compound and a promising candidate for an n-type material. CaIn_2S_4 is characterized by a suitable bandgap, high stability, and good visible-light photocatalytic performance, which is, however, limited because of the easy recombination of the photogenerated carriers [30–32]. However, in the carrier transfer path of a typical direct S-scheme heterojunction, the high oxidation capacity and the strong reduction ability of the photogenerated electrons are retained, resulting in a higher photocatalytic activity [33].

In this work, the photocatalytic performance of the synthesized photocatalyst is improved by achieving synergistic catalysis through the employment of the two strategies of surface oxygen vacancy modification and heterojunction construction. We report the construction of a new, well-designed 2D/2D $\text{CaIn}_2\text{S}_4/\text{BiOCl}$ S-scheme heterojunction by high-temperature calcination combined with a solvothermal method. The visible-light photocatalytic activity of the material was assessed by the degradation of phenol. According to the results, the obtained photocatalyst demonstrates a better performance than pure CaIn_2S_4 and BiOCl, which is attributed to the synergistic effect between SOVs and the surface heterojunction. Based on the proven advantages, the applied strategy and methods can be used to design and construct other similar photocatalytic systems to fully utilize the abundant solar energy.

2. Results and Discussion

2.1. Structure and Morphology of As-Synthesized $\text{CaIn}_2\text{S}_4/\text{BiOCl}$ -SOVs (CIS/BOC-SOVs) Heterojunction

Figure 1 presents the XRD patterns of as-synthesized samples. The diffraction peak positions and corresponding crystal faces of the prepared BiOCl and BOC-SOVs can be indexed to JCPDS 06-0249.34 Pure BiOCl and all calcined samples exhibit main diffraction peaks attributed to (101), (110), (102), (200), (201), (113), (211), and (212) [34]. The diffraction peak planes (311), (400), (511), (440), and (533) of JCPDS 16-0341 standard card correspond

to CaIn_2S_4 . However, the XRD pattern of the CIS/BOC-SOVs samples did not contain any characteristic diffraction peaks of CaIn_2S_4 , which may be ascribed to low crystallinity and loading or a high dispersion of CaIn_2S_4 . Similar results have been found in CaIn_2S_4 -based heterojunction materials, such as $g\text{-C}_3\text{N}_4/\text{CaIn}_2\text{S}_4$ and $\text{CaIn}_2\text{S}_4/\text{Ag}_3\text{PO}_4$ [35,36].

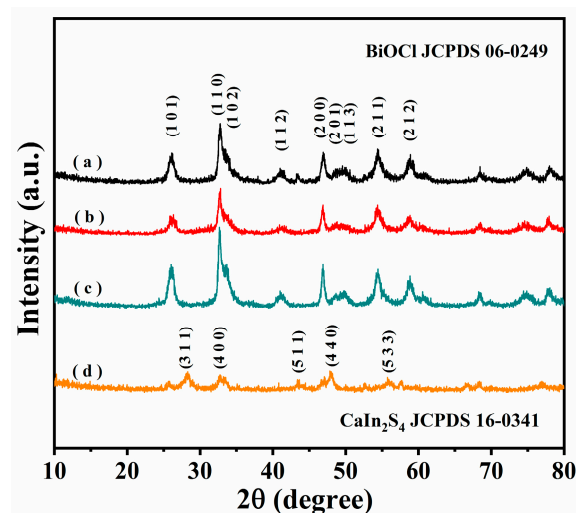


Figure 1. XRD patterns of (a) pure BiOCl, (b) BOC-SOVs, (c) 1% CIS/BOC-SOVs, and (d) pure CaIn_2S_4 .

The composition and surface valence state of the as-synthesized catalysts are investigated by XPS (Figures 2 and 3). The XPS survey spectrum confirms the presence of the main elements in the samples: Bi, O, and Cl in BiOCl, Ca, In, and S in CaIn_2S_4 , and Bi, O, Cl, Ca, In, and S in the surface of the composite sample (Figure 2). As shown in Figure 3a, the peaks at 159.1 eV and 164.3 eV can be attributed to Bi $4f_{7/2}$ and Bi $4f_{5/2}$, confirming that Bi exists in the positive trivalent state [37,38]. As presented in Figure 3b, the three energy bands of the O 1s XPS spectrum are located at 529.8, 531.4, and 533.1 eV, which are respectively attributed to lattice oxygen, vacancy oxygen, and absorbed oxygen [39–41]. In the high-resolution Cl 2p spectra (Figure 3c), two peaks at 197.80 and 199.48 eV can be assigned to Cl $2p_{3/2}$ and Cl $2p_{1/2}$, respectively [41–43]. On the basis of peak-differentiation-imitating analysis, two splitting peaks with binding energies of 351.03 and 347.26 eV were in accordance with Ca $2p_{3/2}$ and Ca $2p_{1/2}$ of Ca^{2+} (Figure 3d) [44,45]. As shown in Figure 3e, the characteristic peaks at 444.53 and 452.09 eV are assigned to In $3d_{5/2}$ and In $3d_{3/2}$, respectively [46–48]. Unfortunately, the presence of S was not observed, probably because the peak positions of S and Bi are too similar. The binding energy of the BiOCl composition element obtained after calcination is shifted, which may be due to the generation of SOVs. It is worth noting that the peaks in the high-resolution XPS spectra of all composite materials have slightly shifted compared with the pure samples, which may be due to the interaction force between heterojunctions. Under visible-light irradiation, the photogenerated charge carriers in the photocatalyst will migrate and transfer, which will lead to the change of the binding energy of the component elements. The binding energy of semiconductor elements that obtain electrons decreases, and in contrast, the binding energy of semiconductor elements that lose electrons increases [49,50]. The shifts may be caused by a partial electron transfer from CaIn_2S_4 to BOC-SOVs caused by Schottky barrier, which would decrease the electron density of CaIn_2S_4 , leading to a shift of the peaks of Bi 4f, O 1s, and Cl 2p for 1% CIS/BOC-SOVs to the direction of higher binding energy, which provides support for the construction of a S-Scheme heterojunction.

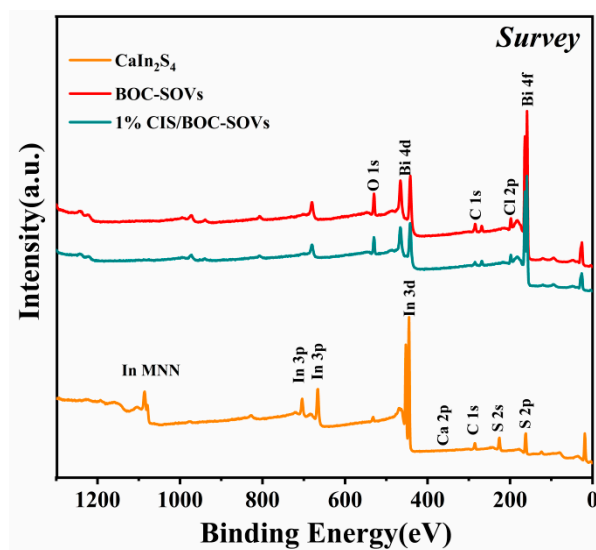


Figure 2. XPS survey spectrum pure BiOCl, pure CaIn_2S_4 and 1 wt% CIS/BOC-SOVs.

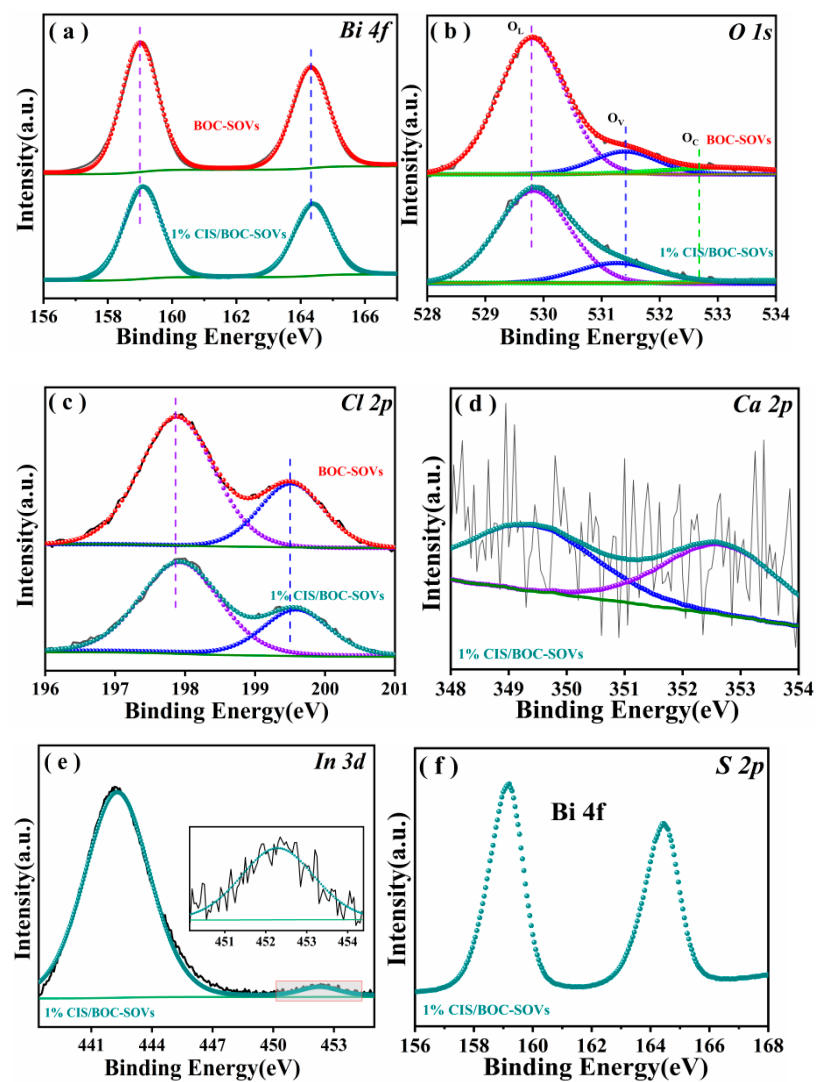


Figure 3. XPS spectra of (a) Bi 4f, (b) O 1s, (c) Cl 2p, (d) Ca 2p, (e) In 3d, and (f) S 2p.

The morphologies of CaIn_2S_4 , BiOCl , and the 1% CIS/BOC-SOVs heterojunction composite were also investigated, and the results are given in Figure 4. Pure CaIn_2S_4 (Figure 4a) exhibits a three-dimensional spherical shape and is composed of a large number of stacked two-dimensional nanosheets, which is consistent with previous reports [45–48]. BiOCl (Figure 4b) has a special nanosheet-like morphology, but obvious agglomeration can be noted. After solvothermal reaction (Figure 4c), BiOCl and CaIn_2S_4 were successfully combined into a 2D/2D heterojunction structure by in-situ growth, which maintained a morphology similar to BiOCl . The corresponding EDX mapping images (Figure 4d–j) indicate that a total of six elements, i.e., Bi, O, Cl, Ca, In, and S, are uniformly distributed on the sample surface. TEM was employed to further analyze the microstructure of the samples. The TEM images shown in Figure 5a,b reveal a spherical structure composed of nanosheets for pure CaIn_2S_4 , which is the same result as obtained by SEM. In Figure 5c, a two-dimensional lamellar structure attributed to BOC-SOVs can be observed. The high-resolution TEM image of 1% CIS/BOC-SOVs (Figure 5d) shows the formation of a two-dimensional nanosheet structure. The lattice spacing of 0.266 nm and 0.327 nm is assigned to BiOCl and CaIn_2S_4 belonging to (102) and (311) crystal planes, respectively (Figure 5e) [50,51]. The existence of BiOCl and CaIn_2S_4 at a visible interface (Figure 5f) reveals the successful preparation of the 2D/2D heterojunction.

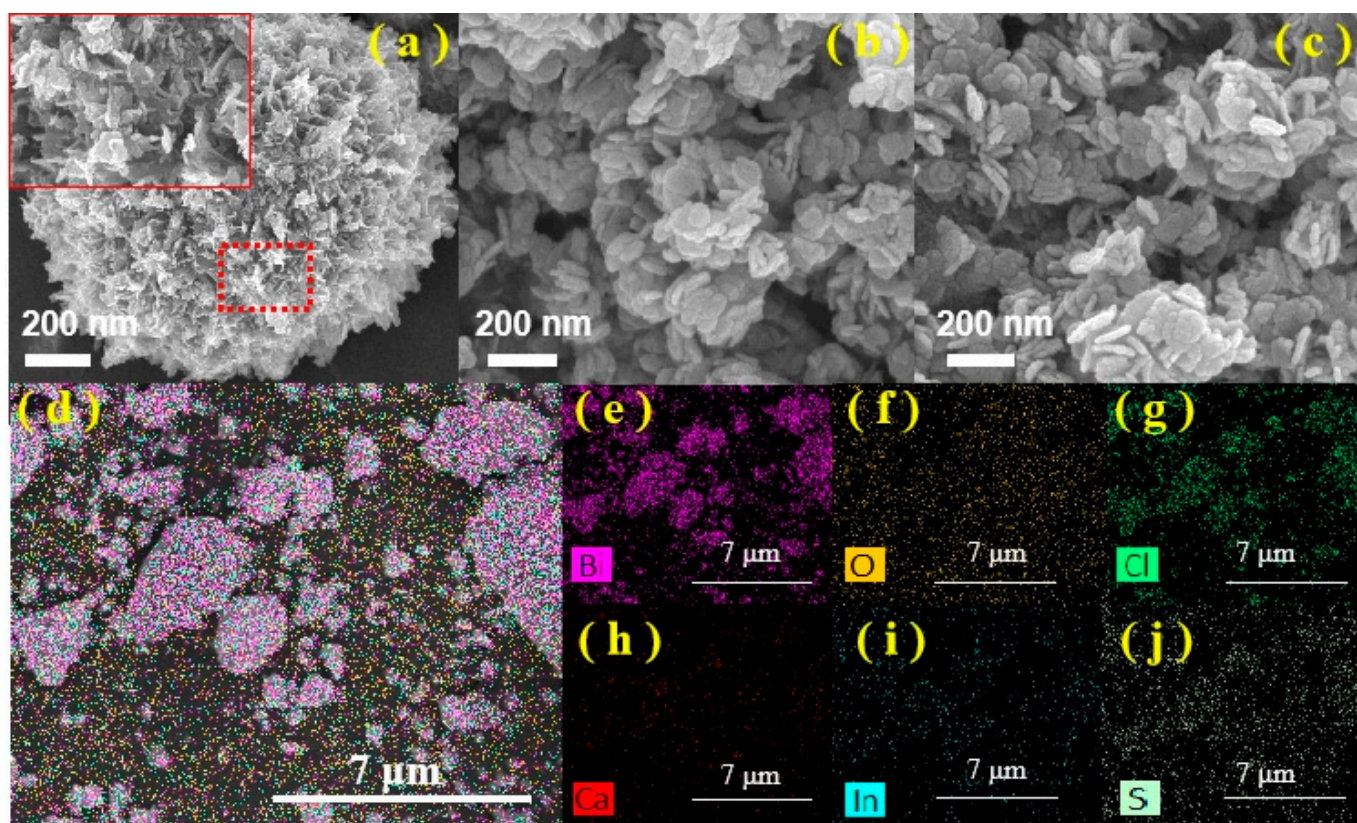


Figure 4. SEM images (a) pure CaIn_2S_4 , (b) pure BiOCl , (c) 1% CIS/BOC-SOVs, (d–j) EDX of 1% CIS/BOC-SOVs.

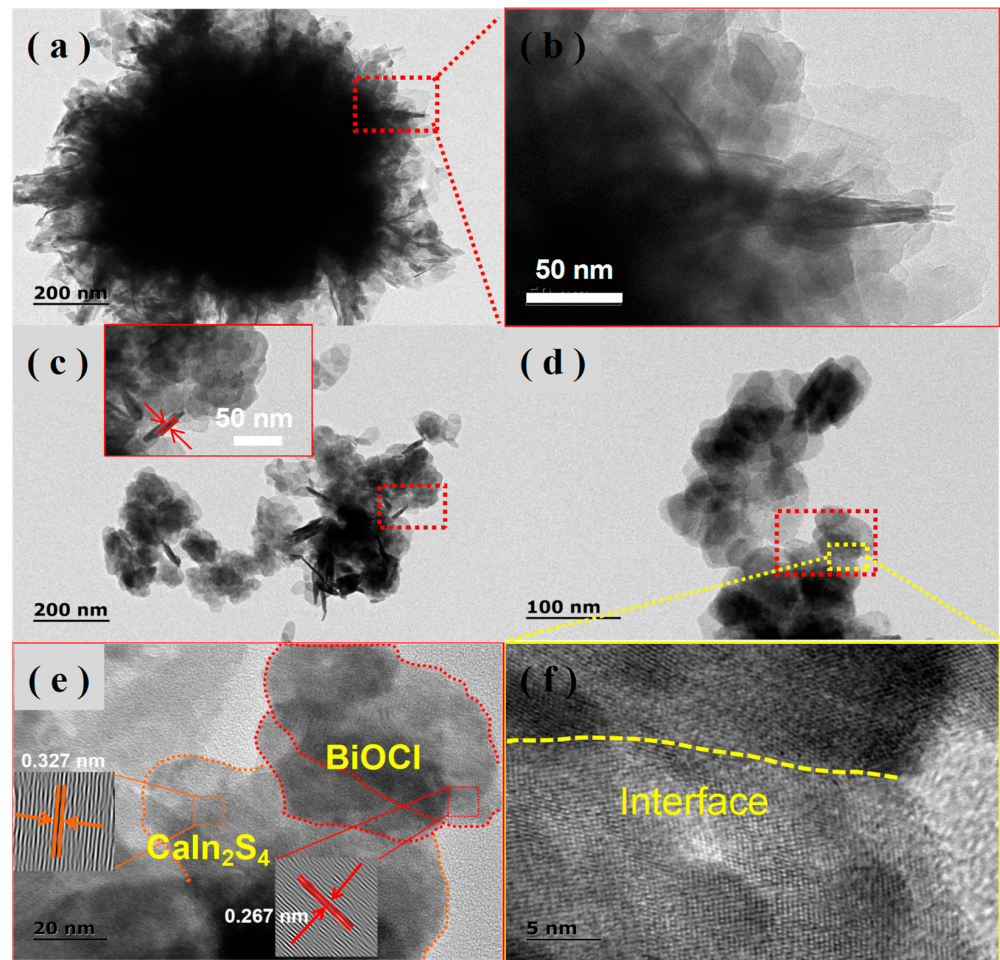


Figure 5. TEM image of (a,b) CaIn_2S_4 , (c) BOC-SOVs, (d–f) 1% CIS/BOC-SOVs.

2.2. Formation of Surface Oxygen Vacancies

While distinct lattice streaks can be observed in the high-resolution TEM photograph of pure BiOCl , the edges of the lattice fringes become indistinct in BOC-SOVs (Figure 6a,b), which illustrates the destruction of the surface structure and the formation of SOVs. The room-temperature ESR spectra (Figure 6c) confirm the presence of oxygen vacancies in BOC-SOVs and 1% CIS/BOC-SOVs ($g = 2.0002$) [51–53]. The signal strength of 1% CIS/BOC-SOVs significantly exceeds the one of BOC-SOVs indicating a higher oxygen vacancy concentration, which is consistent with the results in Table 1.

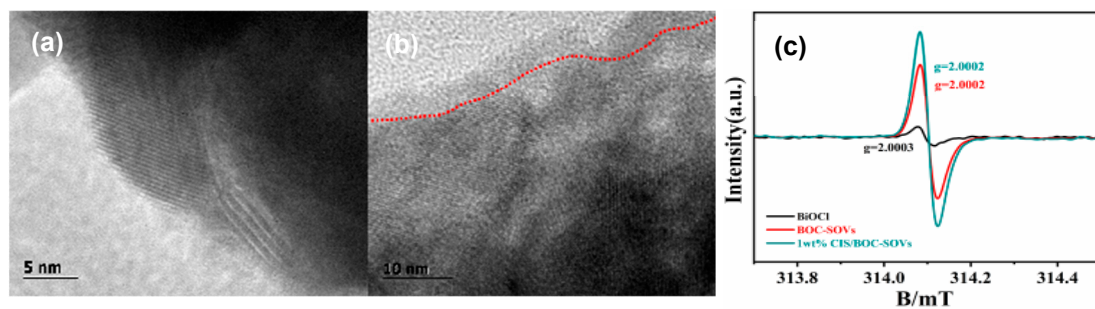


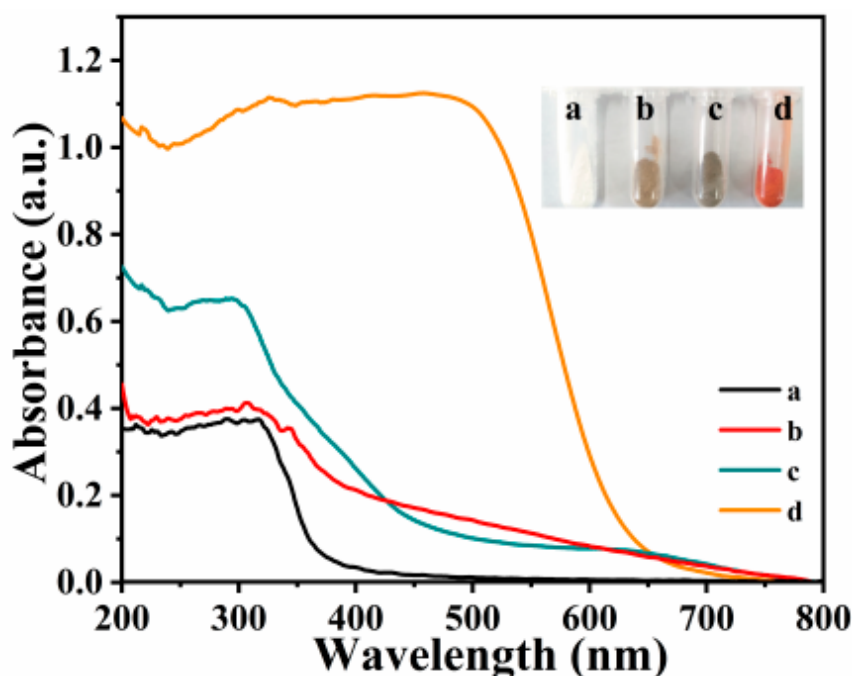
Figure 6. HR-TEM of (a) BiOCl and (b) BOC-SOVs, (c) EPR spectra of BiOCl , BOC-SOVs, and 1% CIS/BOC-SOVs.

Table 1. Ratio of OV/OL of the BOC-SOVs sample compared with that of the 1% CIS/BOC-SOVs sample.

O 1s	529.8 eV, O _L (%)	531.4 eV, O _V (%)	O _V /O _L
BOC-SOVs	80.12	13.02	0.16
1 wt% CIS/BOC-SOVs	77.15	19.67	0.25

2.3. Optical Property and Photocatalytic Activities of CIS/BOC-SOVs

The UV-Vis DRS of the synthesized catalysts are displayed in Figure 7. While the light absorption wavelength at 365 nm can be clearly attributed to BiOCl, which can only absorb ultraviolet light, the light absorption range of BiOCl after calcination containing SOVs is widened to visible light. CaIn₂S₄ exhibits a strong absorption range in the visible light region with the maximum absorption wavelength of about 620 nm. In 1% CIS/BOC-SOVs, the absorption maximum of CaIn₂S₄ at the CaIn₂S₄/BiOCl 2D/2D heterojunction shows a significant red shift compared with BiOCl with SOVs.

**Figure 7.** UV-Vis DRS of (a) pure BiOCl, (b) BOC-SOVs, (c) 1% CIS/BOC-SOVs, and (d) pure CaIn₂S₄.

The photocatalytic performance of the prepared photocatalysts is evaluated by degrading phenol under visible-light irradiation, as shown in Figure 8. Under the exposure of visible light, the concentration of phenol, which possesses a very stable molecular structure, hardly changes, and the adsorption of phenol by the catalyst is almost negligible. According to the results, the calcination temperature and time exhibit a great influence on the photocatalytic activity of BiOCl. A temperature increase from 200 to 400 °C causes an increase in the degradation rate from 50.0% to 23.6%. The degradation rate decreased to 28.9% for BOC-400. Comparing the catalytic performance of catalysts obtained after different calcination times reveals that the catalyst calcined for 1 h demonstrates the highest activity with a degradation rate of 63.4% and a reaction rate constant of 0.0265 min⁻¹. The concentration of OVs depends on the calcination temperature and time. However, too many OVs will become the photogenerated electron/hole recombination center and cause electron-hole annihilation, which results in decreasing the photocatalytic activity.

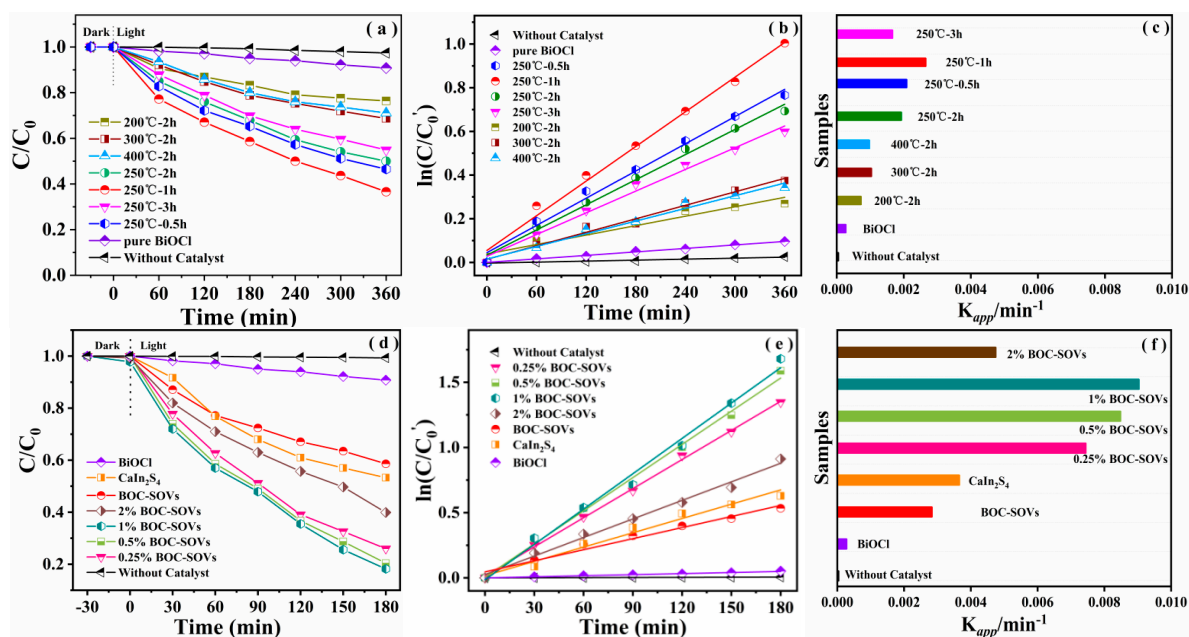


Figure 8. (a,d) Photocatalytic degradation curve, (b,e) corresponding kinetic curves, and (c,f) kinetic rate constant of phenol degradation over different catalysts.

The loading amount of CaIn_2S_4 emerges as another very important factor for the photocatalytic activity of the material. The performance of heterojunction catalyst constructed on the basis of calcination treatment is shown in Figure 8d–f. As evident from the results, 1% CIS/BOC-SOVs showed a higher activity than the other prepared catalysts. The amount of degraded phenol increased to 81.8%, and its apparent rate constant (K_{app}/min^{-1}) improved by a factor of 32.8, 3.2, and 2.47 compared with pure BiOCl, BOC-SOVs, and CaIn_2S_4 , respectively. The enhanced photocatalytic activity of the BiOCl-SOV- CaIn_2S_4 heterojunction can be attributed to the synergistic effect between oxygen vacancies and the 2D/2D heterojunction. As evident from Figure 9a, the synthesis of the heterojunction significantly improved the photocatalytic degradation of phenol by BiOCl. In addition, the UV-Vis absorption spectra (Figure 9b) recorded during the oxidative degradation of p-nitrophenol indicate a certain but slow degradation catalyzed by CIS/BOC-SOVs. A photostability test of the catalyst was performed by the cyclic degradation of phenol. In the XRD pattern displayed in Figure 9c, no obvious new peaks or significant decrease in intensity are observed after the cycle test, which proves the durability of the prepared material.

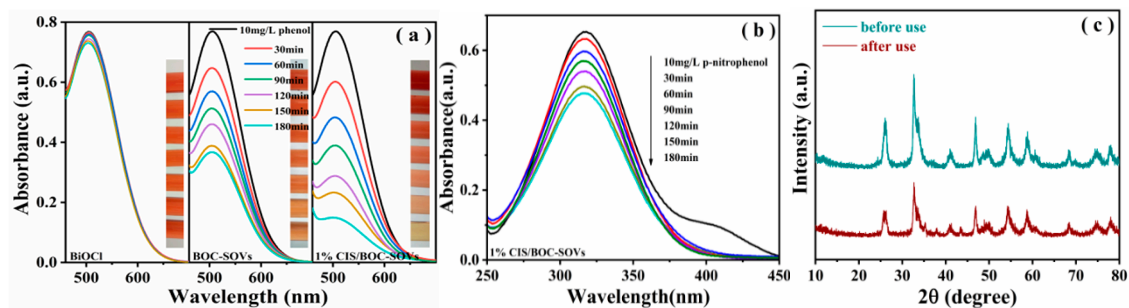


Figure 9. Removal and temporal evolution of UV-Vis absorption spectra of (a) phenol and (b) p-nitrophenol over different catalysts, (c) XRD pattern of 1% CIS/BOC-SOVs before and after use.

2.4. Photocatalytic Mechanism

To evaluate the recombination rate of carriers in the semiconductor photocatalysts, the PL spectra were recorded (Figure 10a). It is worth noting that the CIS/BOC-SOVs

heterojunction exhibits a lower PL intensity than pure BiOCl and BOC-SOVs, indicating that this material possesses a lower electron and hole recombination rate. This result is further confirmed by TR-PL measurement techniques (Figure 10b), where the heterojunction composite demonstrates an enhanced charge carrier lifetime of 1.223 ns versus 1.434 ns of pure BiOCl and 2.148 ns of BOC-SOVs. Table 2 details the various parameters fitted by a double exponential function. Transient photocurrent response measurements and EIS Nyquist plot analysis (Figure 10c,d) were conducted to investigate the separation efficiency of photogenerated carriers in the photocatalysts. The photocurrent generated by the CIS/BOC-SOVs heterojunction is significantly higher than that of other samples including BiOCl or BOC-SOVs, while the same material exhibits the smallest arc radius in the Nyquist plots of these synthesized catalysts. The intrinsic resistance values R_1 of pure BiOCl, BOC-SOVs, and $\text{CaIn}_2\text{S}_4/\text{BiOCl}$ are similar, but the charge transfer resistance R_2 of $\text{CaIn}_2\text{S}_4/\text{BiOCl}$ is small, which indicates that the construction of the heterojunction is more beneficial to the transfer of charge at the interface of the photocatalyst [54,55]. According to these results, the synthesized CIS/BOC-SOVs heterojunction possesses a strong carrier separation ability and low recombination rate due to the tight contact interface, which endows the CIS/BOC-SOVs heterojunction with high catalytic performance.

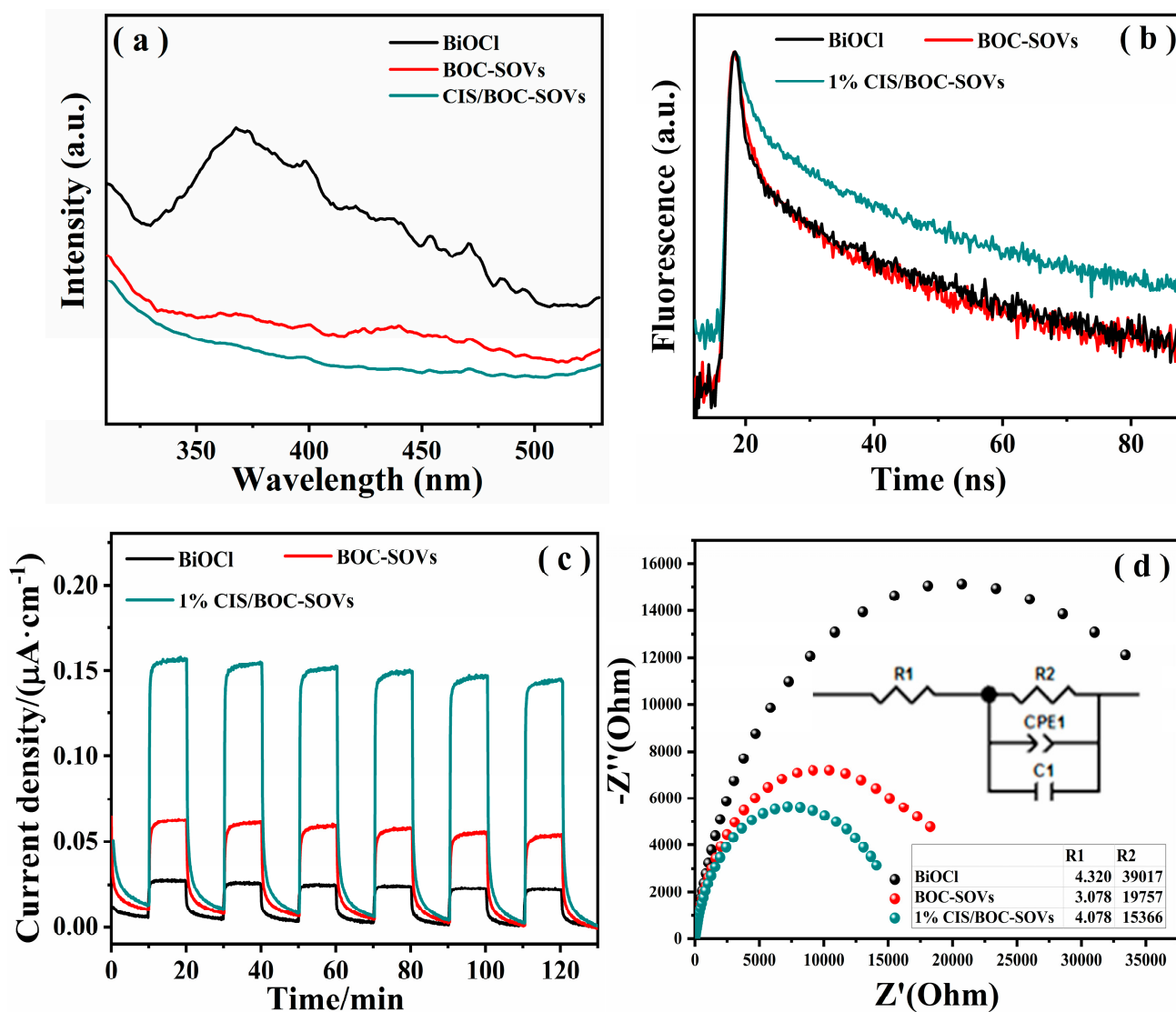
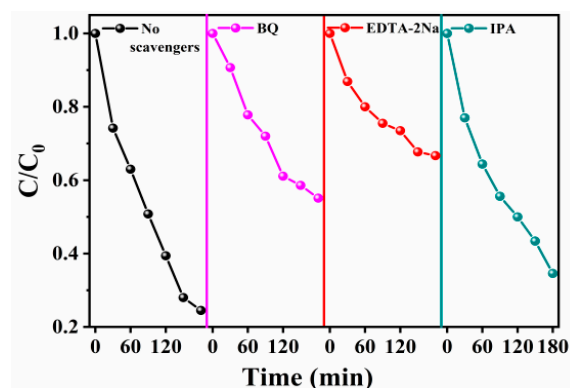
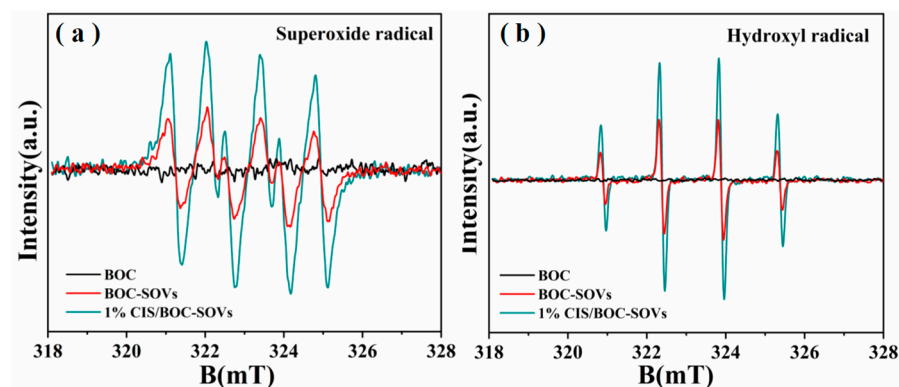


Figure 10. (a) Photoluminescence spectra, (b) Time-resolved fluorescence decay spectra, (c) Transient photocurrent response, and (d) Electrochemical impedance spectroscopy of BiOCl, BOC-SOVs, and 1% CIS/BOC-SOVs.

Table 2. Charge life according to time-resolved transient PL decay curves.

Samples	A1	τ_1/nm	A2	τ_2/nm	$\tau_{\text{av}}/\text{nm}$
BiOCl	1360.5	21.417	6.18×10^{10}	1.223	1.223
BOC-SOVs	1.50×10^3	19.215	1.39×10^9	1.434	1.434
1% BOC-SOVs	1.11×10^7	2.094	2064.6	25.938	2.148

The catalyst with heterojunction demonstrates an outstanding photocatalytic activity for phenol degradation, which may be attributed to the generation of free radicals and holes with strong oxidation ability during photocatalytic degradation. As shown in Figure 11, the presence of IPA and TEA or BQ capture agent caused different inhibitory effects on phenol degradation, which increased in the order EDTA-2Na, BQ, and IPA. In-situ ESR technology was used to detect the free radicals generated during the photocatalytic reaction (Figure 12). The characteristic peaks of $\text{DMPO}\cdot\text{O}_2^-$ and $\text{DMPO}\cdot\text{OH}$ are not detected with pure BiOCl under visible-light irradiation, but the existence of $\cdot\text{O}_2^-$ and $\cdot\text{OH}$ radicals is confirmed for both BOC-SOVs and 1% CIS/BOC-SOVs. It is worth noting that the spectra for the heterojunction catalyst show higher free-radical signal intensities than that of BiOCl and BOC-SOVs. The capture test and the ESR results confirm that the active species involved in the photodegradation of phenol are mainly hydroxyl radical, superoxide radical, and hole [52,53].

**Figure 11.** The capture experiments of 1% CIS/BOC-SOVs under visible light.**Figure 12.** DMPO spin-trapping ESR spectra of BiOCl, BOC-SOVs and 1% BOC-SOVs for $\text{DMPO}\cdot\text{O}_2^-$ (a) and $\text{DMPO}\cdot\text{OH}$ (b) under visible light irradiation.

Accordingly, a reasonable photocatalytic mechanism can be proposed as follows. The calculated bandgaps of BOC-SOVs and CaIn_2S_4 are 2.35 V and 3.20 V, respectively (Figure 13a), while the valence band edge values obtained from the XPS valence band (VB) spectra are 1.88 and 1.30 V (Figure 13b–d), respectively. Finally, the conduction band (CB) edge values are -0.47 and -0.53 V, respectively, as calculated by subtracting the bandgap

value from the VB edge value (Table 3). The S-scheme mechanism of photo-generated carrier transfer of CIS/BOC-SOVs heterostructures is proposed based on experiment and theoretical calculation results. As shown in Scheme 1, before the contact, the Fermi level (E_F) of p-type BiOCl is about 0.3 V above VB, while the Fermi level (E_F) of the n-type semiconductor CaIn_2S_4 is about 0.3 V below CBM. Because the energy of BiOCl from E_F to the vacuum level is greater than that of CaIn_2S_4 , BiOCl is negatively and CaIn_2S_4 is positively charged on opposite sides, so that electrons flow from CaIn_2S_4 to BiOCl following the direction of the electric field. When the two materials contact each other to form a heterojunction, the VB of BiOCl moves upward and the CB of CaIn_2S_4 moves in the opposite direction to achieve the Fermi level equilibrium (E_F) of BiOCl and CaIn_2S_4 , thus theoretically forming a typical S-scheme heterojunction instead of a type-II heterojunction [33,49]. When the heterojunction is irradiated by visible light, electrons in BiOCl with a relatively positively charged potential and holes in the VB of CaIn_2S_4 with a relatively negatively charged potential are simultaneously transferred to the oxygen vacancy state of BiOCl near the CB and then rapidly recombined. Finally, the VB of BiOCl with strong oxidation ability and the CB of CaIn_2S_4 with strong reduction ability are retained. Therefore, compared with the type-II heterojunction, the S-scheme photocatalyst can utilize the redox capability of the photocatalyst to its maximum.

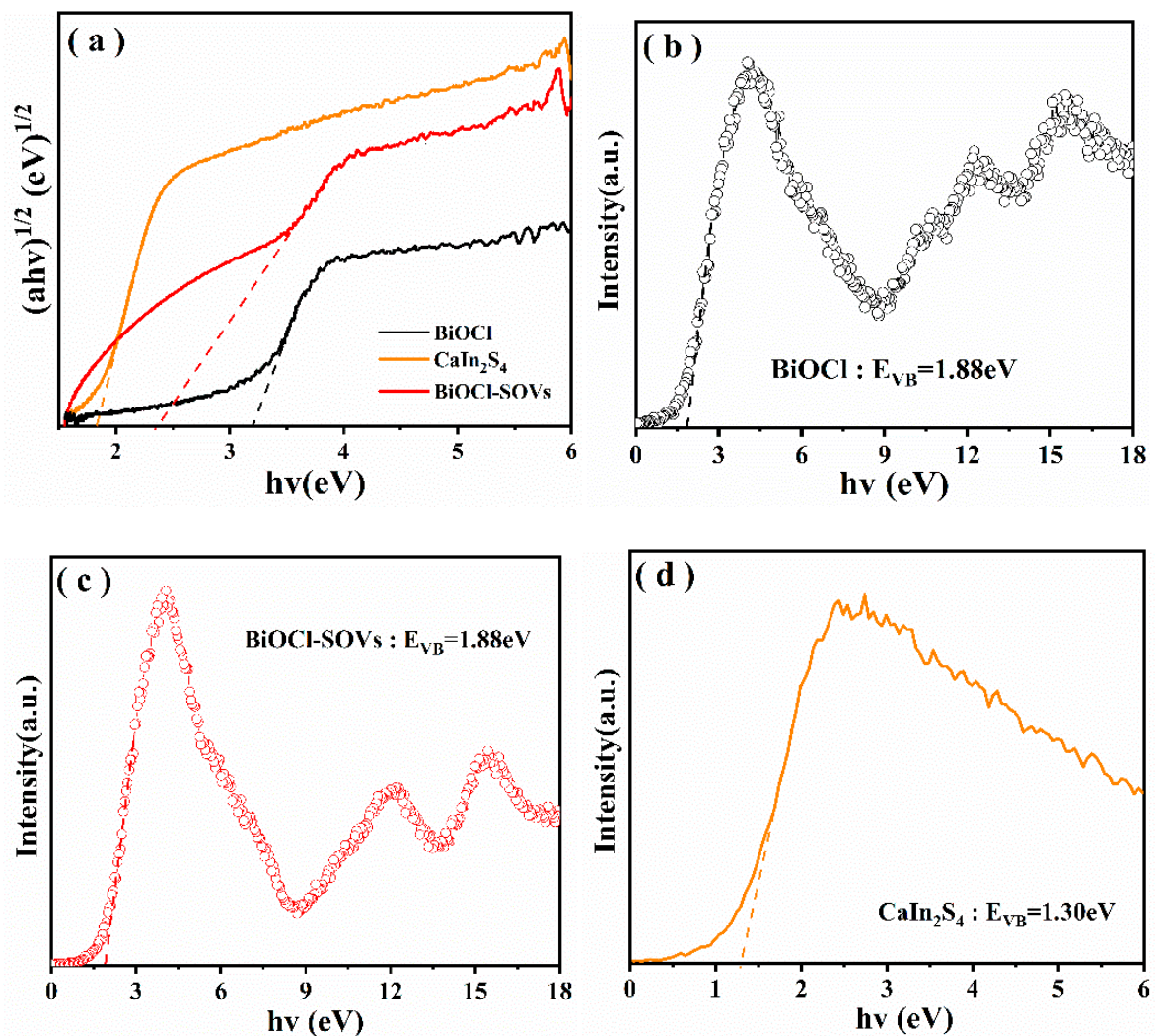
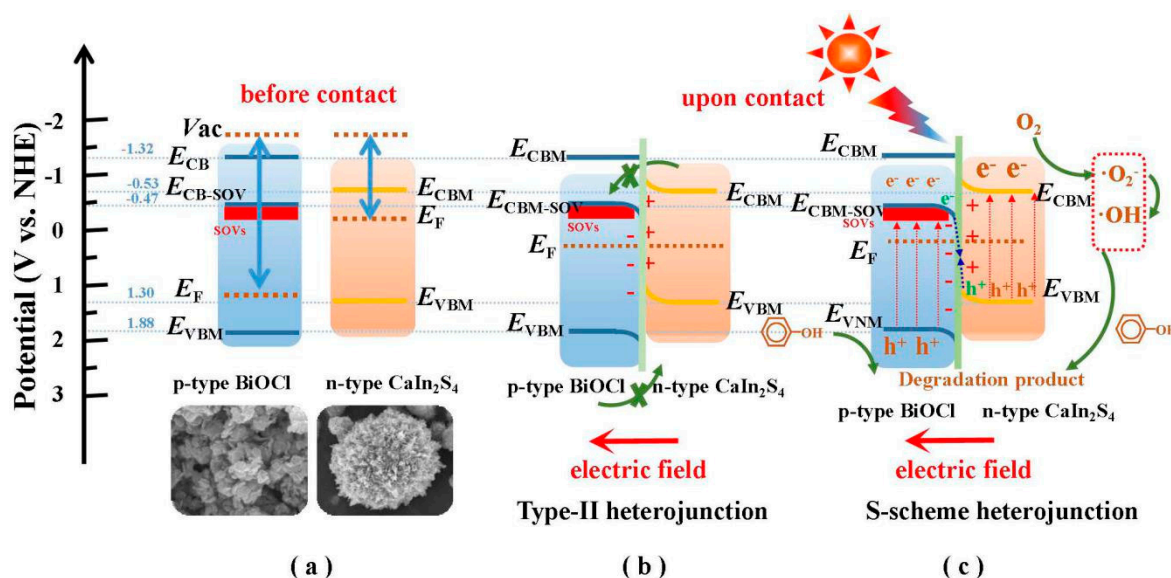


Figure 13. (a,b) The corresponding Tauc curves of BiOCl, BOC-SOVs, and CaIn_2S_4 , and (c,d) VB spectra of the BOC-SOVs and CaIn_2S_4 .

Table 3. The estimated bandgap energy (E_g), conduction band edge (CB), and valence band edge (VB) for BiOCl and CaIn₂S₄.

Semiconductor	Band Gap Energy, E_g (eV)	Conduction Band Edge (CBM, V)	Valence Band Edge (VBM, V)
BiOCl	3.20	-1.32	1.88
BOC-SOVs	2.35	-0.47	1.88
CaIn ₂ S ₄	1.83	-0.53	1.30



Scheme 1. Schematic diagram of the photocatalytic mechanism of charge separation for phenol degradation over 1% CIS/BOC-SOVs under visible-light irradiation. (a) before contact, and upon contact: Type II heterojunction (b), (c) S-scheme charge transfer mechanism. Note: W_I and W_{II} denote the work functions of BiOCl and CaIn₂S₄, respectively. Vac, E_{CBM} , E_{VBM} , and E_F stand for the vacuum level, conduction band minimum, valence band maximum, and Fermi level. The E_{VBM} and E_{CBM} value is given concerning the normal hydrogen electrode (NHE) potential at pH = 7. The VB-XPS determines the E_{VBM} , the E_g of catalysts was estimated by the x-axis intercept obtained from the plot of $(ah\nu)^2$ versus $h\nu$, $E_g = E_{VBM} - E_{CBM}$.

3. Experimental Section

3.1. Chemicals

All reagents were of analytical grade and were used without any further purification. Bismuthnitrate pentahydrate ($\text{Bi}(\text{NO}_3)_3 \cdot 5\text{H}_2\text{O}$), sodium hydroxide (NaOH), thioacetamide ($\text{C}_2\text{H}_5\text{NS}$), ethylene glycol ($\text{C}_2\text{H}_6\text{O}_2$), and ethanol ($\text{C}_2\text{H}_6\text{O}$) were purchased from Tianjin Zhiyuan Chemical Reagent Co., Ltd. (Tianjin, China). Mannitol ($\text{C}_6\text{H}_{16}\text{O}_6$) was purchased from Aladdin Biotechnology Co., Ltd. (Shanghai, China). Calcium nitrate ($\text{Ca}(\text{NO}_3)_2 \cdot 2\text{H}_2\text{O}$) was purchased from Yongsheng Fine Chemical Co., Ltd. (Tianjin, China), Tianjin, China. Indium nitrate ($\text{In}(\text{NO}_3)_3 \cdot 4.5\text{H}_2\text{O}$) was purchased from Sinopharm Chemical Reagent Co., Ltd. (Shanghai, China).

3.2. Sample Preparation

3.2.1. Preparation of BiOCl and Defect-Rich (BOC-SOVs)

Pure BiOCl is prepared by an improved solvothermal method using a previous report [34]. Typically, 0.9702 g (2 mmol) $\text{Bi}(\text{NO}_3)_3 \cdot 5\text{H}_2\text{O}$ and 0.1168 g (2 mmol) NaCl were each dissolved in 10 mL ethylene glycol and magnetically stirred for 30 min to obtain clear and transparent solutions, which were labeled A and B, respectively. Subsequently, 0.1094 g of mannitol and 0.4 g of polyvinylpyrrolidone (PVP) were dissolved in 55 mL water to form solution C. Then, solution A was added dropwise into C under stirring, which continued for 5 min after complete addition before solution B was slowly added dropwise to generate a white precipitate. The mixture was then transferred to a 100 mL high-pressure autoclave

lined with polytetrafluoroethylene for hydrothermal reaction at 160 °C for 8 h. After the reaction finished, the autoclave was allowed to cool to room temperature. After washing with water several times, a certain amount of 15% NaOH was added to adjust the pH to 13. After magnetic stirring was continued for 3 h, it was washed with water to neutrality. Finally, BiOCl powder was obtained after continuous wetting with ethanol, drying at 60 °C for 8 h and grinding. SOVs were generated on the BiOCl (BiOCl-SOVs) by placing pure BiOCl in a muffle furnace, calcining at a certain temperature for a certain time, before allowing it to cool to room temperature. The prepared sample was denoted as BOC-SOVs.

3.2.2. Synthesis of Oxygen-Vacancy-Rich BiOCl-SOVs (BOC-SOVs) Photocatalysts

The BOC-SOVs photocatalysts were prepared through a facile calcination method. Firstly, 1.0 g of pure BOC-SOVs samples prepared above were calcined in a muffle furnace at 200 °C, 250 °C, 300 °C and 400 °C in an air-rich atmosphere for 2 h at a heating rate of 2 °C min⁻¹ to obtain the final BOC-SOVs samples with different temperatures, and the optimum calcination temperature was determined to be 250 °C. In addition, to investigate the effect of calcination time on the photocatalytic activities of the series of BOC-SOVs samples, with 250 °C photocatalysts, the calcination temperature was fixed at 250 °C, and the calcination time was changed to 0.5 h, 1 h, 2 h, and 3 h. The resultant products were denoted as 250 °C–0.5 h, 250 °C–1 h, 250 °C–2 h, 250 °C–3 h, respectively.

3.2.3. Preparation of 2D/2D S-Scheme CaIn₂S₄/BiOCl-SOVs (CIS/BOC-SOVs)

Firstly, 1 g of as-prepared BOC-SOVs was dispersed in 30 mL deionized water, and 0.0076 g thioacetamide (C₂H₅NS) was added followed by ultrasonic treatment for 40 min. Thereafter, 0.0192 g In(NO₃)₃ and 0.0059 g Ca(NO₃)₃ were added, and the mixture was stirred for 1 h. The obtained suspension was transferred to a 50 mL reaction vessel for reaction at 160 °C for 12 h. After the reaction, the system was allowed to cool to room temperature, and the obtained solid was washed with water and alcohol for four times, then dried at 60 °C and ground to obtain 1 wt% CaIn₂S₄/BOC-SOVs, which is denoted as 1% CIS/BOC-SOVs. Following a similar procedure, the weight ratio of CaIn₂S₄ deposited onto the BOC-SOVs was controlled at 0.25, 0.5, 1, and 2 wt%. The obtained samples were denoted as X% CIS/BOC-SOVs (X = 0, 0.25, 0.5, 1, and 2). For comparison, pure CaIn₂S₄ was synthesized by the same method without adding BOC-SOVs.

3.3. Characterization

X-ray diffraction (XRD) was performed on a XRD-7000 instrument (Shimadzu Corp., Kyoto, Japan). X-ray photoelectron spectroscopy (XPS) was carried out with a PHI-5400 (Physical Electronics, Inc., Minnesota, MN, USA) 250 xi system using Al K α radiation as the excitation source. The morphology of the sample was assessed with a JSM-6700F scanning electron microscope (SEM) (JEOL Ltd., Kyoto, Japan) and a JEM-2100 transmission electron microscope (TEM) (JEOL Ltd., Kyoto, Japan). Energy-dispersive X-ray (EDX) analysis was performed on a JSM-7610F field emission SEM (JEOL Ltd., Kyoto, Japan). The UV-Vis diffuse reflectance spectra (UV-Vis DRS) were recorded on a UV-2550 UV-Vis spectrophotometer (Shimadzu Corp., Kyoto, Japan) with barium sulfate (BaSO₄) as reference. The photoluminescence (PL) spectra of samples were obtained on a F-4600 spectrophotometer (Hitachi High-Tech Corp., Kyoto, Japan). The electron spin resonance (ESR) spectra were obtained on a Bruker LEXSYS-II E500 ESR spectrometer (Bruker, Germany) equipped with a quanta-ray Nd: YAG laser system as the irradiation source ($\lambda \geq 420$ nm). Time-resolved photoluminescence (TR-PL) spectra were recorded on a FLS920 fluorescence spectrometer (Edinburgh Instruments Ltd., Edinburgh, UK).

3.4. Photocatalytic Activity Measurement

Photocatalytic phenol degradation: The photocatalytic activity of the catalyst was investigated with colorless phenol as the simulated pollutant, dissolved in ultrapure water in an initial concentration of about 10 mg/L, under irradiation by a 300 W metal halide

lamp as the visible-light source ($\lambda \geq 420$ nm). In the degradation experiment, 200 mg of catalyst was added to a 500 mL reactor containing 200 mL of the phenol solution and then stirred in the dark for about 30 min to ensure that the adsorption-desorption equilibrium was reached. At certain intervals, the supernatant was taken out by a pipette gun and centrifuged to remove residual catalyst. The phenol concentration of the solution was obtained by measuring the UV–Vis absorbance.

4. Conclusions

In this work, 2D/2D $\text{CaIn}_2\text{S}_4/\text{BiOCl}$ -SOVs S-scheme heterojunction materials have been successfully prepared by a simple high-temperature calcination process combined with a solvothermal method and fully characterized by various characterization techniques. The as-prepared photocatalysts demonstrated a highly enhanced photodegradation of phenol under visible-light irradiation with the 1% CIS/BOC-SOVs heterojunction material as the catalyst, with the best photocatalytic activity and a 32.8 times higher photocatalytic rate constant than pure BiOCl. The effective separation of photogenerated electron-hole pairs in a S-scheme heterostructure system can improve the photocatalytic performance of the composite material in the photocatalytic oxidative degradation process, to which SOVs of the heterojunction in multicomponent composite systems contribute significantly. In the degradation reaction, the three main active substances confirmed by ESR spectra and the capture experiment are OH, O_2^- , and h^+ . This paper showed that 2D/2D S-scheme heterojunctions are potential candidates for the degradation of refractory pollutants.

Author Contributions: Z.Z. and Y.Z. designed the experiments and wrote the paper; X.H. and L.G. performed the experiments and analyzed the data; D.W. and K.L. designed the experiments. All authors have read and agreed to the published version of the manuscript.

Funding: This work was financially supported by the National Natural Science Foundation of China (No. 22168040, 21663030, 21666039 & 51672312) and the Open Project of Chongqing Key Laboratory of Inorganic Special Functional Materials, Yangtze Normal University (No. KFKT202001) and Natural Science Basic Research Program of Shaanxi (2020JQ-791) and Graduate Innovation Project of Yan'an University (YCX2020005).

Data Availability Statement: Not applicable.

Conflicts of Interest: The authors declare no conflict of interest.

References

1. Huang, D.; Wang, X.; Zhang, C.; Zeng, G.; Peng, Z.; Zhou, J.; Cheng, M.; Wang, R.; Hu, Z.; Qin, X. Sorptive Removal of Ionizable Antibiotic Sulfamethazine from Aqueous Solution by Graphene Oxide-coated Biochar Nanocomposites: Influencing Factors and Mechanism. *Chemosphere* **2017**, *186*, 414–421. [[CrossRef](#)]
2. Guo, X.; Peng, Z.; Huang, D.; Xu, P.; Zeng, G.; Zhou, S.; Gong, X.; Cheng, M.; Deng, R.; Yi, H. Biotransformation of Cadmium-sulfamethazine Combined Pollutant in Aqueous Environments: Phanerochaete Chrysosporium bring Cautious Optimism. *Chem. Eng. J.* **2018**, *347*, 74–83. [[CrossRef](#)]
3. Li, C.; Chen, G.; Sun, J.; Rao, J.; Han, Z.; Hu, Y.; Xing, W.; Zhang, C. Doping Effect of Phosphate in Bi_2WO_6 and Universal Improved Photocatalytic Activity for Removing Various Pollutants in Water. *Appl. Catal. B Environ.* **2016**, *188*, 39–47. [[CrossRef](#)]
4. Hu, C.; Huang, D.; Zeng, G.; Min, C.; Gong, X.; Wang, R.; Xue, W.; Hu, Z.; Liu, Y. The Combination of Fenton Process and Phanerochaete chrysosporium for The Removal of Bisphenol A in River Sediments: Mechanism Related to Extracellular Enzyme, Organic Acid and Iron. *Chem. Eng. J.* **2018**, *338*, 432–439. [[CrossRef](#)]
5. Hong, Y.; Li, C.; Zhang, G.; Meng, Y.; Yin, B.; Zhao, Y.; Shi, W. Efficient and Stable Nb_2O_5 Modified g- C_3N_4 Photocatalyst for Removal of Antibiotic Pollutant. *Chem. Eng. J.* **2016**, *299*, 74–84. [[CrossRef](#)]
6. Nielsen, L.; Zhang, P.; Bandosz, T. Adsorption of Carbamazepine on Sludge/fish Waste Derived Adsorbents: Effect of Surface Chemistry and Texture. *Chem. Eng. J.* **2015**, *267*, 170–181. [[CrossRef](#)]
7. Chung, S.; Chang, Y.; Choi, J.; Baek, K.; Hong, S.; Yun, S.; Lee, S. Photocatalytic Degradation of Chlorophenols Using Star Block Copolymers: Removal Efficiency, By-products and Toxicity of Catalyst. *Chem. Eng. J.* **2013**, *215–216*, 921–928. [[CrossRef](#)]
8. Omeroglu, A.C.; Ozcan, A.S.; Erdogan, Y.; Ozcan, A. Characterization of *Punica granatum*, L. Peels and Quantitatively Determination of Its Biosorption Behavior towards Lead (II) Ions and Acid Blue 40. *Colloids Surf. B Biointerfaces* **2012**, *100*, 197–204. [[CrossRef](#)] [[PubMed](#)]
9. Deng, J.; Zhang, X.; Zeng, G.; Gong, J.; Niu, Q.; Liang, J. Simultaneous Removal of Cd(II) and Ionic Dyes from Aqueous Solution Using Magnetic Graphene Oxide Nanocomposite as An Adsorbent. *Chem. Eng. J.* **2013**, *226*, 189–200. [[CrossRef](#)]

10. Gong, J.; Wang, B.; Zeng, G.; Yang, C.; Niu, C.; Niu, Q.; Zhou, W.; Liang, Y. Removal of Cationic Dyes from Aqueous Solution Using Magnetic Multi-wall Carbon Nanotube Nanocomposite as Adsorbent. *J. Hazard. Mater.* **2009**, *164*, 1517–1522. [[CrossRef](#)]
11. Chen, F.; Yang, Q.; Li, X.; Zeng, G.; Wang, D.; Niu, C.; Zhao, J.; An, H.; Xie, T.; Deng, Y. Hierarchical Assembly of Graphene-bridged $\text{Ag}_3\text{PO}_4/\text{Ag}/\text{BiVO}_4$ (040) Z-scheme Photocatalyst: An Efficient, Sustainable and Heterogeneous Catalyst with Enhanced Visible-light Photoactivity towards Tetracycline Degradation under Visible Light Irradiation. *Appl. Catal. B Environ.* **2017**, *200*, 330–342. [[CrossRef](#)]
12. Liang, C.; Niu, C.; Guo, H.; Huang, D.; Wen, X.; Yang, S.; Zeng, G. Combination of Efficient Charge-separation Process with The Assistance of Novel Dual Z-scheme System: Self-assembly Photocatalyst of $\text{Ag}@\text{AgI}/\text{BiOI}$ Modified Oxygen-doped Carbon Nitride Nanosheet with Enhanced Photocatalytic Performance. *Catal. Sci. Technol.* **2018**, *8*, 1161–1175. [[CrossRef](#)]
13. Ling, Z.; Wang, W.; Sun, S.; Dong, J.; Gao, E. Selective Transport of Electron and Hole Among {001} and {110} Facets of BiOCl for Pure Water Splitting. *Appl. Catal. B Environ.* **2015**, *162*, 470–474.
14. Lin, H.; Ding, L.; Pei, Z.; Zhou, Y.; Long, J.; Deng, W.; Wang, X. Au Deposited BiOCl with Different facets: On Determination of The Facet-induced Transfer Preference of Charge Carriers and The Different Plasmonic Activity. *Appl. Catal. B Environ.* **2014**, *160–161*, 98–105. [[CrossRef](#)]
15. Guan, M.; Xiao, C.; Zhang, J.; Fan, S.; An, R.; Cheng, Q.; Xie, J.; Zhou, M.; Ye, B.; Xie, Y. Vacancy Associates Promoting Solar-driven Photocatalytic Activity of Ultrathin Bismuth Oxychloride Nanosheets. *J. Am. Chem. Soc.* **2013**, *135*, 10411–10417. [[CrossRef](#)] [[PubMed](#)]
16. Xiong, J.; Cheng, G.; Li, G.; Qin, F.; Chen, R. Well-crystallized Square-like 2D BiOCl Nanoplates: Mannitol-assisted Hydrothermal Synthesis and Improved Visible-light-driven Photocatalytic Performance. *RSC Adv.* **2011**, *1*, 1542–1553. [[CrossRef](#)]
17. Ye, L.; Jin, X.; Leng, Y.; Su, Y.; Xie, H.; Liu, C. Synthesis of Black Ultrathin BiOCl Nanosheets for Efficient Photocatalytic H_2 Production under Visible Light Irradiation. *J. Power Sources* **2015**, *293*, 409–415. [[CrossRef](#)]
18. Yu, Y.; Cao, C.; Liu, H.; Li, P.; Wei, F.; Jiang, Y.; Song, W. A Bi/BiOCl Heterojunction Photocatalyst with Enhanced Electron-hole Separation and Excellent Visible Light Photodegrading Activity. *J. Mater. Chem.* **2014**, *2*, 1677–1681. [[CrossRef](#)]
19. Li, H.; Zhang, L. Oxygen Vacancy Induced Selective Silver Deposition on The {001} Facets of BiOCl Single-crystalline Nanosheets for Enhanced Cr(VI) and Sodium Pentachlorophenate Removal under Visible Light. *Nanoscale* **2014**, *6*, 7805–7810. [[CrossRef](#)]
20. Hu, Z.; Li, K.; Wu, X.; Wang, N.; Li, X.; Li, Q.; Li, L.; Lv, K. Dramatic Promotion of Visible-light Photoreactivity of TiO_2 Hollow Microspheres towards NO Oxidation by Introduction of Oxygen Vacancy. *Appl. Catal. B Environ.* **2019**, *256*, 117860. [[CrossRef](#)]
21. Ma, J.; Wu, H.; Liu, Y.; He, H. Photocatalytic Removal of NO_x over Visible Light Responsive Oxygen-deficient TiO_2 . *J. Phys. Chem. C* **2014**, *118*, 7434–7441. [[CrossRef](#)]
22. Li, H.; Li, J.; Ai, Z.; Jia, F.; Zhang, L. Oxygen Vacancy-mediated Photocatalysis of BiOCl: Reactivity, Selectivity and Perspectives. *Angew. Chem. Int. Ed.* **2018**, *57*, 122–138. [[CrossRef](#)] [[PubMed](#)]
23. Yu, J.; Yu, J.; Ho, W.; Jiang, Z.; Zhang, L. Effects of F-doping on the Photocatalytic Activity and Microstructures of Nanocrystalline TiO_2 Powders. *Chem. Mater.* **2002**, *14*, 3808–3816. [[CrossRef](#)]
24. Li, Y.; Wu, X.; Ho, W.; Lv, K.; Li, Q.; Li, M.; Lee, S. Graphene-induced Formation of Visible-light-responsive $\text{SnO}_2\text{-Zn}_2\text{SnO}_4$ Z-scheme Photocatalyst with Surface Vacancy for The Enhanced Photoreactivity towards NO and Acetone Oxidation. *Chem. Eng. J.* **2018**, *336*, 200–210. [[CrossRef](#)]
25. Su, J.; Zhang, T.; Wang, L. Engineered WO_3 Nanorods for Conformal Growth of $\text{WO}_3/\text{BiVO}_4$ Core-shell Heterojunction towards Efficient Photoelectrochemical Water Oxidation. *J. Mater. Sci.-Mater.* **2017**, *28*, 4481–4491. [[CrossRef](#)]
26. Liu, C.; Yang, Y.; Li, W.; Li, J.; Li, Y.; Chen, Q. In Situ Synthesis of Bi_2S_3 Sensitized WO_3 Nanoplate Arrays with Less Interfacial Defects and Enhanced Photoelectrochemical Performance. *Sci. Rep.* **2016**, *6*, 23451. [[CrossRef](#)] [[PubMed](#)]
27. Fu, J.; Chang, B.; Tian, Y.; Xi, F.; Dong, X. Novel $\text{C}_3\text{N}_4\text{-CdS}$ Composite Photocatalysts with Organic-inorganic Heterojunctions: In Situ Synthesis, Exceptional Activity, High Stability and Photocatalytic Mechanism. *J. Mater. Chem. A* **2013**, *1*, 3083–3090. [[CrossRef](#)]
28. Bafaqeer, A.; Tahir, M.; Amin, N.A. Synergistic Effects of 2D/2D ZnV_2O_6 /RGO Nanosheets Heterojunction for Stable and High Performance Photo-induced CO_2 Reduction to Solar Fuels. *Chem. Eng. J.* **2018**, *334*, 2142–2153. [[CrossRef](#)]
29. Tonda, S.; Kumar, S.; Gawli, Y.; Bhardwaj, M.; Ogale, S. $g\text{-C}_3\text{N}_4$ (2D)/CdS (1D)/rGO (2D) Dual-interface Nano-composite for Excellent and Stable Visible Light Photocatalytic Hydrogen Generation. *Int. J. Hydrogen Energy* **2017**, *42*, 5971–5984. [[CrossRef](#)]
30. Ding, J.; Li, X.; Chen, L.; Zhang, X.; Tian, X. Photocatalytic Hydrogen Production Over Plasmonic AuCu/ CaIn_2S_4 Composites with Different AuCu Atomic Arrangements. *Appl. Catal. B Environ.* **2018**, *224*, 322–329. [[CrossRef](#)]
31. Jiang, D.; Li, J.; Xing, C.; Zhang, Z.; Meng, S.; Chen, M. Two-Dimensional $\text{CaIn}_2\text{S}_4/g\text{-C}_3\text{N}_4$ Heterojunction Nanocomposite with Enhanced Visible-Light Photocatalytic Activities: Interfacial Engineering and Mechanism Insight. *ACS Appl. Mater. Interfaces* **2015**, *7*, 19234–19242. [[CrossRef](#)]
32. Ding, J.; Yan, W.; Sun, S.; Bao, J.; Gao, C. Hydrothermal Synthesis of CaIn_2S_4 -Reduced Graphene Oxide Nanocomposites with Increased Photocatalytic Performance. *ACS Appl. Mater. Interfaces* **2014**, *6*, 12877–12884. [[CrossRef](#)] [[PubMed](#)]
33. Zhang, L.; Cheng, B.; Fan, J.; Yu, J. S-Scheme Heterojunction Photocatalyst. *Chem* **2020**, *6*, 1–17.
34. Myung, Y.; Wu, F.; Banerjee, S.; Park, J.; Banerjee, P. Electrical Conductivity of p-Type BiOCl Nanosheets. *Chem. Commun.* **2015**, *51*, 2629–2632. [[CrossRef](#)] [[PubMed](#)]
35. Yuan, W.; Yang, S.; Li, L. Synthesis of $g\text{-C}_3\text{N}_4/\text{CaIn}_2\text{S}_4$ Composites with Enhanced Photocatalytic Activity under Visible Light Irradiation. *Dalton Trans.* **2015**, *44*, 16091–16098. [[CrossRef](#)]

36. Wan, S.; Ou, M.; Zhong, Q.; Zhang, S. Z-scheme $\text{CaIn}_2\text{S}_4/\text{Ag}_3\text{PO}_4$ Nanocomposite with Superior Photocatalytic NO Removal Performance: Fabrication, Characterization and Mechanistic Study. *New J. Chem.* **2018**, *42*, 318–326. [[CrossRef](#)]
37. Wang, X.; Zhao, Y.; Li, F.; Li, Y.; Zhao, J.; Hao, Y. A Chelation Strategy for In-situ Constructing Surface Oxygen Vacancy on {001} Facets Exposed BiOBr Nanosheets. *Sci. Rep.* **2016**, *6*, 24918. [[CrossRef](#)] [[PubMed](#)]
38. Zhao, Z.; Zhou, Y.; Wang, F.; Zhang, K.; Yu, S.; Cao, K. Polyaniline-decorated {001} Facets of $\text{Bi}_2\text{O}_2\text{CO}_3$ Nanosheets: In Situ Oxygen Vacancy Formation and Enhanced Visible Light Photocatalytic Activity. *ACS Appl. Mater. Interfaces* **2015**, *7*, 730–737. [[CrossRef](#)]
39. Chen, Y.; Yang, W.; Gao, S.; Sun, C.; Qi, L. Synthesis of Bi_2MoO_6 Nanosheets with Rich Oxygen Vacancies by Postsynthesis Etching Treatment for Enhanced Photocatalytic Performance. *ACS Appl. Nano Mater.* **2018**, *1*, 3565–3578. [[CrossRef](#)]
40. Wang, Q.; Wang, W.; Zhong, L.; Liu, S.; Cao, X.; Cui, F. Oxygen Vacancy-rich 2D/2D $\text{BiOCl-g-C}_3\text{N}_4$ Ultrathin Heterostructure Nanosheets for Enhanced Visible-light-driven Photocatalytic Activity in Environmental Remediation. *Appl. Catal. B Environ.* **2018**, *220*, 290–302. [[CrossRef](#)]
41. Zeng, R.; Luo, Z.; Su, L.; Zhang, L.; Tang, D.; Niessner, R.; Dietmar, K.D. Palindromic Molecular Beacon Based Z-scheme BiOCl-Au-CdS Photoelectrochemical Biodetection. *Anal. Chem.* **2019**, *91*, 2447–2454. [[CrossRef](#)]
42. Tian, F.; Li, G.; Zhao, H.; Chen, F.; Li, M.; Liu, Y.; Chen, R. Residual Fe Enhances the Activity of BiOCl Hierarchical Nanostructure for Hydrogen Peroxide Activation. *J. Catal.* **2019**, *370*, 265–273. [[CrossRef](#)]
43. Singh, P.; Priya, B.; Shandilya, P.; Raizada, P.; Singh, N.; Pare, B.; Jonnalagadda, S. Photocatalytic Mineralization of Antibiotics using 60% WO_3/BiOCl Stacked to Graphene Sand Composite and Chitosan. *Arab. J. Chem.* **2019**, *12*, 4627–4645. [[CrossRef](#)]
44. Ding, J.; Hong, B.; Luo, Z.; Sun, S.; Bao, J.; Gao, C. Mesoporous Monoclinic CaIn_2S_4 with Surface Nanostructure: An Efficient Photocatalyst for Hydrogen Production under Visible Light. *J. Phys. Chem. C* **2014**, *118*, 27690–27697. [[CrossRef](#)]
45. Ding, J.; Li, X.; Chen, L.; Zhang, X.; Yin, H.; Tian, X. Site-selective Deposition of Reductive and Oxidative Dual Cocatalysts to Improve the Photocatalytic Hydrogen Production Activity of CaIn_2S_4 with Surface Nanostep Structure. *ACS Appl. Mater. Interfaces* **2019**, *11*, 835–845. [[CrossRef](#)] [[PubMed](#)]
46. Wan, S.; Ou, M.; Cai, W.; Zhang, S.; Zhong, Q. Preparation, Characterization and Mechanistic Analysis of $\text{BiVO}_4/\text{CaIn}_2\text{S}_4$ Hybrids that Photocatalyze NO Removal under Visible Light. *J. Phys. Chem. Solids* **2018**, *122*, 239–245. [[CrossRef](#)]
47. Wang, X.; Li, X.; Liu, C.; Li, F.; Li, Y.; Zhao, J.; Liu, R.; Li, G. Metalloid Ni_2P and Its Behavior for Boosting the Photocatalytic Hydrogen Evolution of CaIn_2S_4 . *Int. J. Hydrogen Energy* **2018**, *43*, 219–228. [[CrossRef](#)]
48. Liu, B.; Liu, X.; Li, L.; Zhu, G.Z.; Li, Y.; Li, C.; Gong, Y.; Niu, L.; Xu, S.; Sun, C. CaIn_2S_4 decorated WS_2 Hybrid for Efficient Cr (VI) Reduction. *Appl. Surf. Sci.* **2019**, *484*, 300–306. [[CrossRef](#)]
49. Zhen, Y.; Yang, C.; Shen, H.; Xue, W.; Gu, C.; Feng, J.; Zhang, Y.; Fu, F.; Liang, Y. Photocatalytic performance and mechanism insights of a S-scheme $\text{g-C}_3\text{N}_4/\text{Bi}_2\text{MoO}_6$ heterostructure in phenol degradation and hydrogen evolution reactions under visible light. *Phys. Chem. Chem. Phys.* **2020**, *22*, 26278–26288. [[CrossRef](#)]
50. Xu, F.; Zhang, J.; Zhu, B.; Yu, J.; Xu, J. CuInS_2 Sensitized TiO_2 Hybrid Nanofibers for Improved Photocatalytic CO_2 Reduction. *Appl. Catal. B Environ.* **2018**, *230*, 194–202. [[CrossRef](#)]
51. Wang, D.; Shen, H.; Guo, L.; Wang, C.; Fu, F.; Liang, Y. $\text{Ag}/\text{Bi}_2\text{MoO}_6-x$ with Enhanced Visible-light-responsive Photocatalytic Activities via The Synergistic Effect of Surface Oxygen Vacancies and Surface Plasmon. *Appl. Surf. Sci.* **2018**, *436*, 536–547. [[CrossRef](#)]
52. Hu, J.; Li, J.; Cui, J.; An, W.; Liu, L.; Liang, Y.; Cui, W. Surface Oxygen Vacancies Enriched $\text{FeOOH}/\text{Bi}_2\text{MoO}_6$ Photocatalysis-fenton Synergy Degradation of Organic Pollutants. *J. Hazard. Mater.* **2020**, *384*, 121399. [[CrossRef](#)] [[PubMed](#)]
53. Zhang, S.; Pu, W.; Chen, A.; Xu, Y.; Wang, Y.; Yang, C.; Gong, J. Oxygen Vacancies Enhanced Photocatalytic Activity towards VOC_s Oxidation over Pt Deposited Bi_2WO_6 under Visible Light. *J. Hazard. Mater.* **2020**, *384*, 121478. [[CrossRef](#)] [[PubMed](#)]
54. Guo, H.; Zhu, Q.; Wu, X.; Jiang, Y.; Xie, X.; Xu, A. Oxygen Deficient ZnO_{1-x} Nanosheets with High Visible Light Photocatalytic Activity. *Nanoscale* **2015**, *7*, 7216–7223. [[CrossRef](#)] [[PubMed](#)]
55. Du, X.; Song, S.; Wang, Y.; Jin, W.; Ding, T.; Tian, Y.; Li, X. Facile one-pot synthesis of defect-engineered step-scheme $\text{WO}_3/\text{g-C}_3\text{N}_4$ heterojunctions for efficient photocatalytic hydrogen production. *Catal. Sci. Technol.* **2021**, *11*, 2734–2744. [[CrossRef](#)]